02,11

Jump quantum phase transitions in a vortex sistem and the dinamic complex magnetic permeability of high-temperature binary $YBa_2Cu_3O_{7-x}$ superconductors

© Kh.R. Rostami

Kotelnikov Institute of Radio Engineering and Electronics (Fryazino Branch), Russian Academy of Sciences, Fryazino, Moscow Oblast, Russia

E-mail: rostami@ms.ire.rssi.ru

Received May 11, 2021
Revised September 5, 2021
Accepted October 15, 2021

A nonlocal high-frequency method for measuring the dynamic complex magnetic permeability with enhanced spatial resolution is developed to simultaneously determine the bulk and local character of stepwise penetration of a magnetic flux through twin boundaries (TBs) into a $YBa_2Cu_3O_{7-x}$ HTSC sample during its stepwise decomposition into twins. By the values of fields corresponding to the regions of steps, the thermodynamic first critical magnetic fields are determined: the penetration of a flux into a sample — a Josephson medium; the development of a critical state in the Josephson medium; the penetration of a flux into twins; and the values of the critical fields of phase transitions in the vortex system of the HTSC sample, such as the melting fields of a vortex crystal, the formation of a superconducting glass state in the sample, and the transition to the vortex glass and Bragg glass states.

Keywords: high-frequency inductance, bulk and local dynamic complex magnetic permeability, magnetic flux trapping, effective demagnetization factor, twins (monodomains, crystallites, sub- and nanocrystallites), twin boundaries.

DOI: 10.21883/PSS.2022.02.53697.107

1. Introduction

Although the physical properties of high-temperature superconductors (HTSCs) have been studied extensively since their discovery [1] and a great amount of experimental and theoretical data have been accumulated, a mechanism of superconductivity providing a consistent interpretation of the obtained results has not been found yet. In addition, the fundamental reasons why the critical current density (J_c) in HTSCs is so low have not been determined conclusively; this precludes one from developing engineering techniques for increasing J_c in HTSC materials. At the same time, it is known that the density of current carriers (holes) in HTSCs ($0.7-1$) $10^{22}\,cm^{-3}$) is an order of magnitude lower than the corresponding value in traditional metallic superconductors, and the coherence length in HTSCs — $\xi \sim 5-10\,Å$ along axis c and $20-35\,Å$ in plane $[ab]$) is, in turn, $5-10$ times lower than the one in metallic superconductors. The studies of a more technologically accessible $YBa_2Cu_3O_{7-x}$ (YBCO) also revealed that even the most perfect single YBCO crystals contain a great number of regularly positioned twin boundaries (TBs) with twinning plane (110). Depending on the method of material preparation, TB width Δd varies approximately from 30 to 50 Å, and distance d between TBs varies within the range of $\sim 200-2000\,Å$ [2–5]. This relation between parameters makes the physical properties of layered HTSCs highly sensitive to minor spatial nonuniformities, since their coherence length is of the same order of magnitude as the TB width and interlayer, interatomic, and interelectron distances. This, in turn, leads to a strong dependence of the magnetotransport properties of HTSCs on the presence of defects (specifically, the density and the spatial distribution of TBs). It should be noted that the presence of TBs is in the very nature of YBCO HTSC, since twin domains (monodomains, crystallites, sub- and nanocrystallites) form as a result of the structural phase transition from the tetragonal (nonsuperconducting) phase to the orthorhombic (superconducting) one at a temperature of $\sim 7000°C$ and/or as a result of alteration of stoichiometry of samples induced by doping [2–10]. Since the properties of TBs are also manifested vividly in other cuprates (the most striking instance is LaSrCuO) and iron pnictides, it is impossible to get rid of them, and one needs to contend with their presence. The macroscopic properties of HTSCs have been studied fairly well. However, microscopic processes within twins remain understudied, since serious challenges arise in the experimental examination of the magnetotransport properties of twins. The interest in twins and TBs stems from the fact that twins are the more ordered systems with higher degrees of structural perfection and the best critical superconducting parameters, while TBs exert a significant influence on microscopic and macroscopic parameters of YBCO HTSC. In addition, owing to the quantum restriction on the superconducting order parameter at TB, which translates into low values of J_c in the interdomain and intradomain space in HTSCs, the growth of twin boundaries and/or TBs induced by doping

or thermal processing allows one to adjust the electronic properties of HTSCs and retrieve meaningful physical data needed for the development of HTSCs with current values close to Ginzburg–Landau depairing current J^{GL} [11] and quantum devices based on HTSCs [10,12]. For example, the discovery of modulation of superfluid density by TBs in twinned orthorhombic underdoped $Ba(Fe_{1-x}Co_x)_2As_2$ crystals [13–15] has once again made relevant the issue of forming a domain microstructure in the HTSC electron subsystem with the use of TBs and thus producing a nonuniform spatial distribution of the supercurrent carrier density at a TB and near it [15,16]. The observed stripes of increased diamagnetic susceptibility, which vanished in tetragonal overdoped $Ba(Fe_{1-x}Co_x)_2As_2$ crystals, were consistent with enhanced superfluid density at TBs [13,14]. Further validation of the hypothesis of TB-assisted formation of a domain microstructure in the HTSC electron subsystem was performed by exposing twinned domains and TBs to the front of a travelling damped magnetic wave [11,17–19]. This technique made it possible to identify the interface between vortex and Meissner regions (IVMR). The movement of IVMR around a TB provided an opportunity to examine the distribution of supercurrent density near and at a TB as a function of the TB lattice period [11,17–19]. Thus, the development of a highly informative precision superconductor diagnostics technique having a radically different physical basis and providing various ways to (i) identify clearly twins and TBs in all types of YBCO HTSC structures; (ii) examine physical processes in twins near and at a TB; (iii) determine the geometric size and critical parameters of twins; (iv) find out the degree of nonuniformity of HTSC samples; and (v) establish the TB distribution period is likely to be of great academic and applied relevance (see [11,17–19] and references therein). The availability of such an HTSC diagnostics technique should provide an opportunity to establish feedback control over the production cycle of HTSC materials. This would make it possible to control the crystal lattice symmetry in the structural phase transition from the tetragonal phase to the orthorhombic one and control the process of variation of the sample stoichiometry by doping or changing the oxygen content in the crystallization of twins via thermal treatment at $T < 600–700^\circ$C. As a result, this technique would allow for simultaneous examination of the crystal, magnetic, and electronic microstructures of HTSC samples and provide an opportunity to determine the specific features of interaction of these microstructures, thus offering a clue to the understanding of the mechanism of high-temperature superconductivity. We have examined the local characteristics of samples using a Hall sensor (HS) in local (local measurement) and nonlocal (local measurement) field modes in [11,17–19] to reveal TBs and study the physical processes, which provide a clear indication of the presence of TBs on microscales in film and bulk YBSCO HTSC samples, near and at them. The local field acting on the samples in these studies was produced by an oscillating decaying local magnetic field, and a highly stable uniform magnetostatic field was used in the nonlocal mode. In the present study, we propose a more sensitive method with an increased spatial resolution for simultaneous examination of macroscopic and microscopic characteristics of HTSC samples of an arbitrary shape. This method allows one to reveal the bulk and local nature of TB manifestation and involves exposing a sample to a nonlocal highly stable uniform magnetostatic field and performing a nonlocal integral measurement (with the use of high-frequency inductance) of the magnetic response signal in the form of dynamic complex magnetic permeability μ_v. This provides an opportunity to collect comprehensive data on both integral and local characteristics of a sample. With this end in view, the magnetic flux distribution (both at the edge of an HTSC sample and within it) and the interaction between the external magnetic field and screening Meissner currents are examined at different points on the sample surface by scanning the bulk of a sample via IVMR. The developed method for producing a local magnetic field relies on the ZFCMFA (zero field cooling with magnetic flux accumulation) mode to reduce the influence of edge effects, which are significant in measurements in uniform fields, on the local characteristics of samples [11,17–19]. The proposed method is free from drawbacks typical of the technique that utilizes uniform external fields to determine the characteristics of samples with a high demagnetization factor, since the ZFCMFA mode allows one to preadjust the surface energy barrier for vortex lines penetrating a superconductor. It becomes possible to isolate TBs gradually and selectively by trapping the magnetic flux in them and determine a very important characteristic of superconductors: the local energy barrier of formation of a mixed state in a sample [20,21].

In view of the fact that structural analysis with the use of X-ray and electron microscopes without a magnetic field acting simultaneously on a sample provides an opportunity to reveal TBs clearly only in single-crystalline YBCO and in grains of polycrystalline YBCO HTSC and reveals only dislocations, microcracks, pores, and other linear and point defects (as opposed to TBs) in epitaxial YBCO films, the aims of the present study were as follows.

(1) Demonstrate the bulk nature of the stepwise decomposition of a sample into twins with close demagnetization factors (n) resulting in the stepwise penetration of the magnetic flux into YBCO HTSC.

(2) Examine more thoroughly the reasons behind the selective manifestation of TBs in HTSC materials with different microstructures in relation to their synthesis methods and identify the reasons why TBs are revealed in all microstructures only after the application of a magnetic field to an HTSC sample.

(3) Measure the value of critical fields of stepwise quantum phase transitions in the vortex system of a sample using the integral method.

2. Experimental methods and samples

2.1. Samples

In order to determine why TBs are not detected in epitaxial YBCO films by high-resolution microscopes of different types and, on the contrary, are detected in single-crystalline YBCO samples and in grains of polycrystalline YBCO, we studied the magnetic properties of HTSC using YBCO samples with different microstructures and different heights of the edge barrier, bulk pinning, and demagnetization. Disk-shaped samples with a diameter of 8 mm were fabricated from bulk textured (axis c was perpendicular to the sample plane) quasi-single-crystalline polycrystalline YBCO (sample No. 1) and untextured ceramic YBCO and epitaxial YBCO films (samples Nos. 2 and 3) and had a thickness of $\approx 0.7-4.2$ mm and $\approx 0.4-0.5\,\mu$m, respectively. Temperatures $T_c \approx 92$ K and $\Delta T_c \approx 0.6$ K were determined for the epitaxial films, and the bulk sample had $T_c \approx 92$ K and $\Delta T_c \approx 1$ K. The critical temperature was measured using a resonance inductance meter with a sensitivity of $\approx 1\,\mu$H in the frequency range of (355–505) kHz and derived from temperature dependence $\ell(T)$ of the microsolenoid inductance, where $\ell \approx 65\,\mu$H.

2.1.1. Characteristics of the textured quasi-single-crystalline polycrystalline YBCO sample

Textured quasi-single-crystalline polycrystalline YBCO samples were cut with a diamond cutter from a cylindrical blank. Fused textured quasi-single-crystalline samples were synthesized using a seed mounted at the top at high temperature. An optical microscope clearly revealed bright single-crystalline blocks (monodomains) ≈ 0.11 cm^2, which were separated by narrow inclusions of a green tint, in polarized light. This was confirmed by mapping the trapped magnetic flux (TMF) with an HS. End surfaces were removed with a diamond cutter to exclude the nonuniformity of oxygen distribution at end faces (relative to the distribution in the bulk). The critical current measured at $T = 77.4$ K in the terrestrial field using the four-probe method with bridges made from quasi-single-crystalline YBCO samples was $\approx 5.7 \cdot 10^3$ A/cm^2. TBs were observed on the surface of monodomains of quasi-single-crystalline YBCO. The critical current measured at $T = 77.4$ K in the terrestrial field using the four-probe method with a bridge made from a monodomain was $\approx 6 \cdot 10^5$ A/cm^2. The resistance anisotropy measured on the surface of a monodomain was ≈ 3; this implies that a small number of TBs are present in a monodomain. Textured polycrystalline and untextured ceramic samples consisted of twins $\sim 1\,\mu$m in size.

2.1.2. Characteristics of epitaxial YBCO films

Epitaxial YBCO films (sample No. 2) of various thickness with axis $\vec{c}$ oriented perpendicular to the substrate surface were fabricated by DC reactive magnetron sputtering of a stoichiometric high-density YBCO target in oxygen-containing atmosphere under a pressure of 3.5 mbar (350 Pa). Cylindrical $NdGaO_3$ (110) substrates with a diameter of 8 mm and thickness d up to $1\,\mu$m were used. The substrate temperature was 800°C. The results of X-ray diffraction analysis revealed a single orientation: (0001). The FWHM of the rocking curve was 0.2°. The Scherrer formula was used to determine the average size of coherent scattering regions based on the broadening of diffraction line (0005). This size was around 20 nm, which is indicative of the presence of a significant number of small-angle boundaries. Cylindrical epitaxial YBCO films (sample No. 3) with a diameter of 8 mm, thickness h up to $1\,\mu$m, and axis c oriented perpendicular to the substrate surface were also fabricated on an $NdGaO_3$ (110) substrate by laser sputtering of a stoichiometric high-density YBCO target. The results of X-ray diffraction analysis revealed that the films have a low density of defects. The examination with a high-resolution scanning electron microscope (SEM) and current measurements demonstrated that the films are anisotropic in plane ab, and their anisotropy is comparable to the one of a single crystal. The critical current measured at 77.4 K in the terrestrial field using the four-probe method with bridges fabricated by photolithography and wet etching was $\approx 5 \cdot 10^6$ A/cm^2 [22,23]. When structural analysis of epitaxial films is performed using X-ray and electron microscopes without a magnetic field acting simultaneously on a sample, normally only dislocations, microcracks, pores, and other point defects (as opposed to TBs) are revealed clearly. Small TBs are masked in a film by extended TBs and may be identified only when a magnetic field is applied to this film [24,25].

Figure 1 presents the isothermal field dependences of $B_{tr}(H_0)$ for samples Nos. 2 and 3. The close-up of the tail of dependence $B_{tr}(H_0)$ for sample No. 2 fabricated by reactive magnetron sputtering is shown in Fig. 1, *a*. The complete $B_{tr}(H_0)$ dependence is shown in the inset. The dependence for sample No. 3 fabricated by laser sputtering is plotted in Fig. 1, *b*. Steps in the $B_{tr}(H_0)$ dependence can be seen easily in Fig. 1. The estimate for epitaxial films is $B_{tr}^{\max}(0) = J_c d \approx 200$ G for samples Nos. 2 and 3. The obtained results deviate strongly from the experimentally determined $B_{tr}^{\max}(0) \approx 13.04$ G for sample No. 2 (see Fig. 1, *a*) and $B_{tr}^{\max}(0) \approx 1.34$ G for sample No. 3 (see Fig. 1, *b*). The TMF scattering fields in a film close primarily via TBs and other defects within the film. This suggests that, contrary to transport measurements and the X-ray diffractometer and SEM readings, TBs in the studied epitaxial film behave in strong magnetic fields similarly to weak links in polycrystalline films. A high level of TMF density is illustrative of a higher density of defects and a greater number of interdomain (island) extended weak links. This suppresses effects related to TBs and translates into a small amplitude of steps in films fabricated by magnetron sputtering (see Fig. 1, *a*). The TMF density

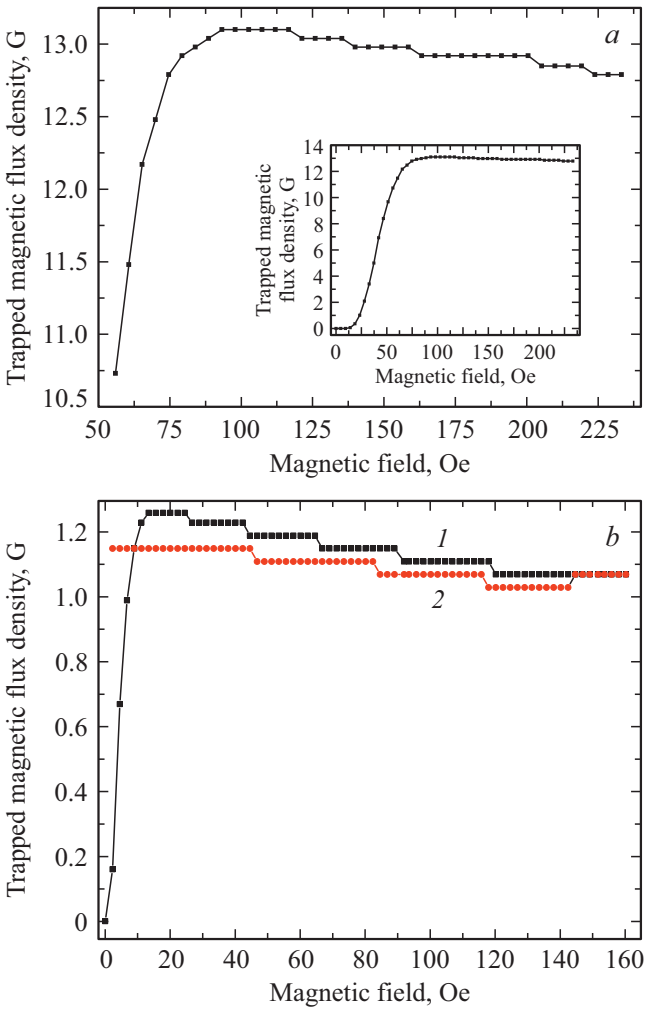

Figure 1. Isothermal field dependences of $B_{tr}(H_0)$ for epitaxial YBCO films. (a) Close-up of the tail of dependence $B_{tr}(H_0)$ for sample No. 2 fabricated by reactive magnetron sputtering. The complete $B_{tr}(H_0)$ dependence is shown in the inset. (b) Dependence for sample No. 3 fabricated by laser sputtering. Films with a diameter of 8 mm, thickness h up to 1 μm, and axis c oriented perpendicular to the substrate surface were deposited onto an $NdGaO_3$ (110) substrate via sputtering of a stoichiometric high-density YBCO target. Temperature $T = 77.4$ K.

in films fabricated by laser sputtering is much lower (see Fig. 1, b), and TBs are manifested more clearly [11,17–19].

2.2. Experiment details

Isothermal field dependences of flux density $B(H_o)$, TMF density $B_{tr}(H_o)$, and dynamic complex magnetic permeability $\mu_v(H_0)$ were studied in ZFC (zero field cooling) and ZFCMFA modes using the following methods:

– nonlocal field — nonlocal measurement: the external field is uniform, and the response signal is recorded by means of the bulk high-frequency complex magnetic permeability;

– nonlocal field — local measurement: the external field is uniform and constant, and the response is detected with an HS.

(a) The ZFC mode — the sample was cooled to liquid nitrogen temperature in zero magnetic field, an external magnetic field step was applied for 5 min, and B_{tr} was measured 5 min after the removal of this field at the center of the sample surface. The sample was then heated to a temperature above T_c, and the experiment was repeated for a different H_o step.

(b) The ZFCMFA mode differs from ZFC in that, following the initial trapping, the next 5-min-long step of field H_o is applied without changing the B_{tr} value and heating the sample, the overall value of B_{tr} is then measured 5 min after the removal of this field, and so on. In the ZFC mode, the application of field step H_0 ensured direct interaction between the magnetic field and the sample in the Meissner state and thus provided an opportunity to examine the macroscopic properties of the sample. In the ZFCMFA mode (see [23,24] and below for details), weak links are destroyed gradually by the scattering fields of vortices trapped in the film, and effort is made to ensure that the external field interacts with separate twins. Thus, in contrast to ZFC that allows one to examine the macroscopic HTSC properties only, ZFCMFA also provides an opportunity to study the physical processes within samples.

The observation of processes of decomposition of a sample into twins, which results in stepwise penetration of the magnetic flux into the sample „dividing“ into twins, with the use of local and nonlocal (integral) methods, the measurement of thermodynamic first critical magnetic fields H_{ic1} of twins, and the comparison of the obtained results are vitally important for the following reasons:

– the joint response of all twins of the sample to total field $H(t)$, which consists of a highly stable uniform magnetostatic field and a variable magnetic field, is taken into account;

– the interaction of Meissner macroscopic and microscopic screening currents induced by the external magnetostatic field and alternating induction currents is studied simultaneously;

– the interaction of all vortices both with each other and with Meissner currents of twins and alternating induction currents is studied simultaneously;

– the response signal is enhanced due to an increase in the number of twins in the group of twins with close n.

Total magnetic field $H(t)$ consisting of a magnetostatic field with magnitude H_o up to 1.6 kOe and a variable magnetic field with magnitude $H_1 \approx 3 \cdot 10^{-3}$ Oe [26] was applied to the sample in order to study the field dependence of dynamic complex magnetic permeability $\mu_v = \mu_v' + i\mu_v''$:

$$H(t) = H_o + H_1 \cos(\omega t + \varphi), \text{ where } H_o \gg H_1.$$

The isothermal field dependence of bulk high-frequency dynamic complex magnetic permeability $\mu_v(H_0) = (B/H_0)(H_0)$ of YBCO sample No. 1 mounted

within a microsolenoid was studied by measuring inductance $L_k(\mu_v, H_0, T, B_{tr})$ of this microsolenoid with a high-frequency resonance inductance meter in the 355−505 kHz frequency range in the ZFCMFA mode. The $L_k(\mu_v, H_0, T, B_{tr})$ measurement procedure was as follows.

The inductance of the solenoid with YBCO sample No. 1 with diameter $D \approx 6$ mm and thickness $h \approx 4.2$ mm was first measured at room temperature. This was done by adjusting capacitance C_k in the L_kC_k circuit until resonance (i.e., the difference between the operating frequency and the resonance frequency became $\Delta f = f_w - f_{res} = 0$) was achieved. The measured L_k value was $\approx 68.53\,\mu$H. The inductance was then measured again after cooling to 77.4 K in zero magnetic field. Owing to diamagnetic screening of the sample, the inductance decreased, and the resonance frequency shifted. The resonance condition with $\Delta f = 0$ in the L_kC_k circuit was established once again by rotating variable capacitor C_k. This condition corresponded to $L_k \approx 37.26\,\mu$H. An uniform constant field step H_0 was applied for 5 min, and resonance frequency shift Δf_u was measured under these conditions. The field was then turned off, and TMF-induced resonance frequency shift Δf_{tr} was measured 5 min after that. The next field step was applied without heating the sample, and the measurement was repeated. The sensitivity of the resonance inductance meter was $\approx 0.1\,\mu$H within the frequency range of $\approx 1.1-1.5$ MHz and $\approx 1\,\mu$H within $\approx 355-505$ kHz.

Dependences $B_{tr}(H_o)$ for samples Nos. 2 and 3 were measured in the ZFC and ZFCMFA modes (with steps of an oscillating local magnetic field decaying in magnitude and a highly stable uniform magnetostatic field ΔH_0 with a magnitude up to 1.6 kG applied to the sample) at liquid nitrogen temperature using an HS with a working area 1.5×0.5, 0.1×0.05 mm^2 in size and conversion coefficients $\approx 80-120\,\mu$V·mT^{-1}. The setup [27,28] detected HS signals with a sensitivity of $\approx 2.5 \cdot 10^{-3}$ G. The magnetic field was perpendicular to the sample surface. Terrestrial field component H_z was compensated by a coil coaxial with the solenoid that set the external magnetic field.

The spatial resolutions of the used methods and the accuracy of measurement of the TB period also depend on the duration of application of a field step and the time delay between the removal of the field and the start of measurement, since the greater t is, the lower is the influence of relaxation processes (the time of flux entry into the sample and the time of its exit) on the measurement result. The rapidly relaxing part of the TMF density is normally exhausted within $t = 5$ min, and a „rigidly" fixed vortex lattice is established in the sample. The performance of the above methods in the ZFCMFA mode is illustrated well by Fig. 2. According to this figure, an artificial magnetic barrier (in the form of demagnetization fields of B_{tr2}) for entry of vortices from the next field step is produced in the sample via the initial magnetic flux trapping. To enable magnetic flux trapping at the next field step, one first needs to compensate the demagnetization fields of B_{tr2}, thus removing the magnetic barrier created earlier, and then to raise the magnetic pressure on screening Meissner currents of twins until the sample decomposes further into smaller groups of twins with close n. The total field of steps was

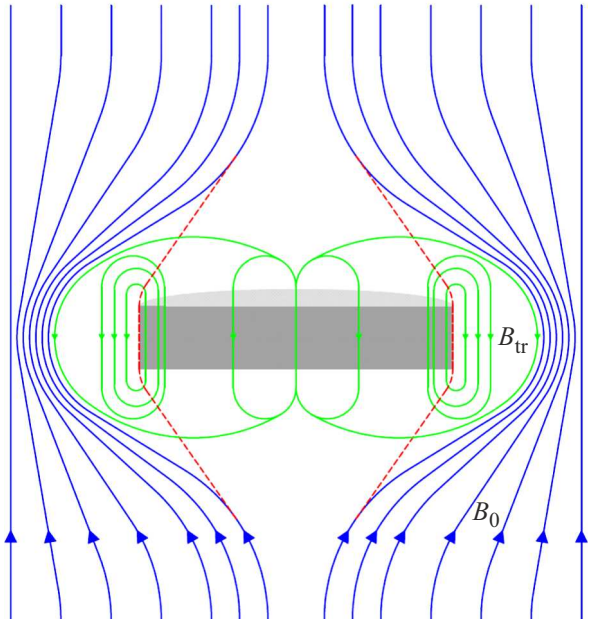

Figure 2. Qualitative diagram illustrating how an artificial magnetic barrier (in the form of demagnetization fields of B_{tr2}) for entry of vortices from the next field step is produced in the sample via the initial magnetic flux trapping.

$$H_{op} - H_{DBtr2} = p\Delta H_o,$$

where H_{DBtr2} is the demagnetization field produced by field B_{tr2}; ΔH_o is the step amplitude of the external magnetic field; and p is the number of steps. In order to simplify the analysis of the obtained data, the amplitude of steps of field H_0 was increased gradually and monotonically by $\Delta H_o \approx 1-50$ Oe (and then reduced in a similar fashion). The initial setting and the gradual summation of steps with predefined H_o provided an opportunity to first fix and then move IVMR and monitor its movement deeper into the sample and into twins (and back). Thus, when probing the bulk of the sample with IVMR, one may examine separately the magnetic state of regions with the same critical parameters, perform „local" flux trapping, alter the TMF topology using the field front, and gradually localize IVMR around the regions (twins and TBs) with the highest critical parameters $(H_{c1i}, J_{ci}, T_{ci})$ by increasing the magnitude of the external field [11,17–19]. Therefore, the spatial resolution of the used methods depends on the set amplitude of field H_0 steps, the magnetometer sensitivity, the duration of application of an external field step, and the time delay between the removal of the field and the start of measurement. A differential local approximation technique [11,17–19] was developed based on the procedure of subtraction of TMF density B_{tr1} measured in the ZFC mode from TMF density B_{tr2} measured in the ZFCMFA

mode. This helped exclude the influence of the surface barrier, edge and bulk pinning, and internal and external demagnetization fields of the sample and twins on the measurement results. The mentioned procedure coupled with the stepwise variation of magnitude H_o of the applied field produced a δ-like spatial TMF distribution. This provided an opportunity to isolate more accurately the components associated with Meissner screening currents of the sample and twins.

3. Results and discussion

Figure 3 shows the isothermal field dependences of the inductance of the microsolenoid with sample No. 1. Inductance $L_{ktr}(H_0) \approx (\Delta f_{tr})(H_0)$ measured with TMF after the removal of the external field in shown in Fig. 3, *a*, and inductance $L_{ku}(H_0) \approx (\Delta_{fu})(H_0)$ measured with the external magnetic field switched on is presented in Fig. 3, *b*. Critical magnetic fields H_{ic1} of twins (at which the sample undergoes stepwise decomposition into groups of twins with close n values [11,17–19]) are seen clearly in the curves of $\Delta f_{tr}(H_0)$ (Fig. 3, *a*) corresponding to both directions of field variation, namely the increasing field (*1*) and the decaying field (*2*). Curves *1* and *2* also feature well-pronounced regions of constant $\Delta f_{tr}(H_0)$ extending along H_0. This indicates that the studied vortex lattice has high elastic moduli. The lattice period undergoes a spontaneous stepwise change only when the sample decomposes into yet another group of twins with close n. Curve *2* for the decaying field also has well-pronounced steps at the first critical magnetic field of penetration of the field into the sample ($H_{c1} \approx 50$ Oe), the field establishing the critical state in the intertwine Josephson space ($H_{tj} \approx 25$ Oe), and the first critical magnetic field of flux penetration into the intertwine Josephson space ($H_{c1j} \approx 0.5$ Oe) [29,30]. The obtained results agree well with literature data [30]. In the region of weak fields, the results reveal clearly the dynamics of formation of a superconducting glass state [31,32] with the corresponding groups of superconducting loops (consisting of twins interconnected by weak Josephson links). These loops have the same values of n and H_{ic1} of flux penetration through weak links within loops. The regular vortex lattice formed in the presence of a field (vortex crystal) melts down after the removal of the external magnetic field, switching to the vortex liquid flow mode [7,8]. As a result of magnetic flux trapping, stepwise quantum phase transitions between vortex states occur in the sample as the field increases: vortex crystal — superconducting glass–vortex glass — Bragg glass [10,33–41]. The specific features in the region of fields of stepwise transitions between the indicated states reveal clearly a series of critical magnetic fields of stepwise quantum transitions $H_{ic1}(Oe) \approx 100$, 110, 125, 175, 225, etc. Curves *1* and *2* in Fig. 3, *a* also allow one to determine H_{ic1} of flux penetration into the sample and its twins and identify regions of almost linear diamagnetic screening. A self-organized Bragg glass state

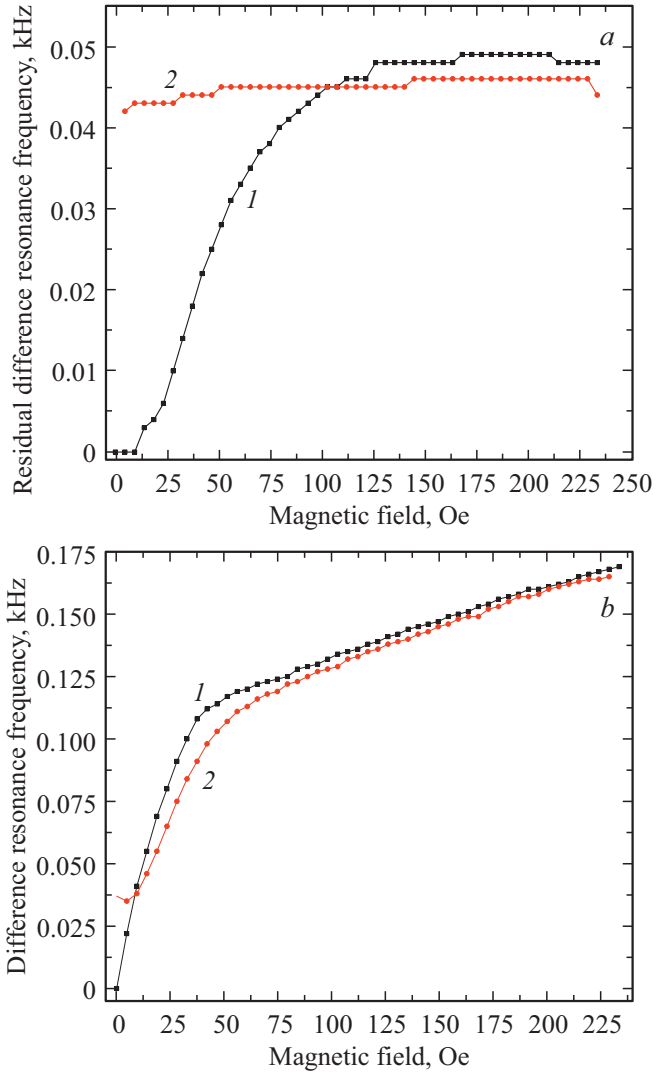

Figure 3. Isothermal field dependences of the inductance with sample No. 1. (*a*) Inductance $L_{ktr}(H_0) \approx (\Delta f_{tr})(H_0)$ measured with TMF after the removal of the external field; (*b*) inductance $L_{ku}(H_0) \approx (\Delta f_u)(H_0)$ measured with the external magnetic field switched on. Curves *1* and *2* correspond to the increasing field and the decaying field, respectively. Temperature $T = 77.4$ K.

emerges spontaneously when the field increases, and regions of an ideal Bragg glass state extended along the field are produced artificially in the decaying field. As the field decreases, large-size hypervortices [42] withdraw from the sample, thus allowing one to monitor the processes of stepwise flux switching in superconducting loops in the region of weak fields (see Fig. 3, *a*, curve *2*). On removal of the field, the formed vortex crystal melts down, and vortex liquid flows in the process of TMF relaxation. Transitions to the state of a superconducting glass and further to the state of a vortex glass occur within 5 min of termination of the rapid-relaxation TMF phase. When the external field decreases from its maximum value, vortices trapped at twin TBs undergo rearrange back along the field. In addition,

Josephson and Abrikosov vortices are trapped once again at intertwine twinning planes and intertwine junction vortices (ITJVs) at points of TB intersection [19]. This results in the formation of phase-dependent codirectional vortex arrays in the sample. As the field decreases further, vortex arrays combine gradually; the resulting vortex array occupies the entire sample volume, and scattering fields of all vortices close around the sample. Thus, as the field increases, the trapped flux switches gradually to centers with stronger pinning, suppressing the trapped flux at centers with weak pinning. This was evidenced by the gradual weakening of magnetic relaxation, which vanished completely when the field increased to a certain level. When the field decreases, the trapped flux is retained at centers with strong pinning, and centers with weak pinning gradually become involved in trapping. Thus, IVMR contracts gradually around the regions with the highest H_{c1i}, J_{ci}, T_{ci} values as the external field increases; when the field decreases, the flux fills the space between these regions, and all nanodipoles reorient and become arranged along the magnetic field. In traditional methods, all pinning centers are simultaneously involved in flux trapping in both increasing and decreasing fields. The study of magnetic relaxation on flux entry into the sample and exit from it revealed that the exponential curve of relaxation of the magnetic flux density has kinks at the points of stepwise division of the sample into twins. The straightened logarithmic relaxation curve was a sum of logarithms with different coefficients. This demonstrates that different groups of twins have differing relaxation rates. The relaxation rate decreased with size of twins and eventually dropped to zero. The spatiotemporal TMF characteristics were examined by varying the distance between the sample and the HS in order to analyze the relaxation rates in different groups of twins. When the distance between the HS and the sample surface varies, the HS gradually becomes sensitive to TMF fragments from different pinning centers closing around different groups of twins, thus allowing one identify different relaxation rates selectively for separate groups of twins.

Figure 4 shows the field dependences of magnetic permeability of sample No. 1. Figure 4, *a* presents dependence $\mu_{vtr}(H_0) = (H_{tr}/H_0)(H_0) \approx (\Delta f_{tr}/H_0)(H_0)$ obtained in the case when the external field is switched off and only TMF is present in the sample, while dependence $\mu_v(H_0) = (B/H_0)(H_0) \approx (\Delta f_u/H_0)(H_0)$ obtained with the external magnetic field switched on is plotted in Fig. 4, *b*. Curves *1* and *2* correspond to the increasing field and the decaying field, respectively. Just as the $\Delta f_{tr}(H_0)$, $\Delta f_u(H_0)$ dependences in Figs. 3, *a, b*, the $\mu_{vtr}(H_0)$, $\mu_v(H_0)$ dependences in Fig. 4, *a, b* have well-pronounced features and jumps of $\mu_{vtr}(H_0)$ and $\mu_v(H_0)$. It can be seen from Fig. 4, *a* that the curves go through their maxima at field H_{ic1}. This is a fine illustration of the fact that the magnetic flux trapping occurs primarily in the extensive interdomain space and in nonsuperconducting regions of the sample. This allows one to separate distinctly the regions of Meissner domains from the interdomain and intertwine regions. The passage of

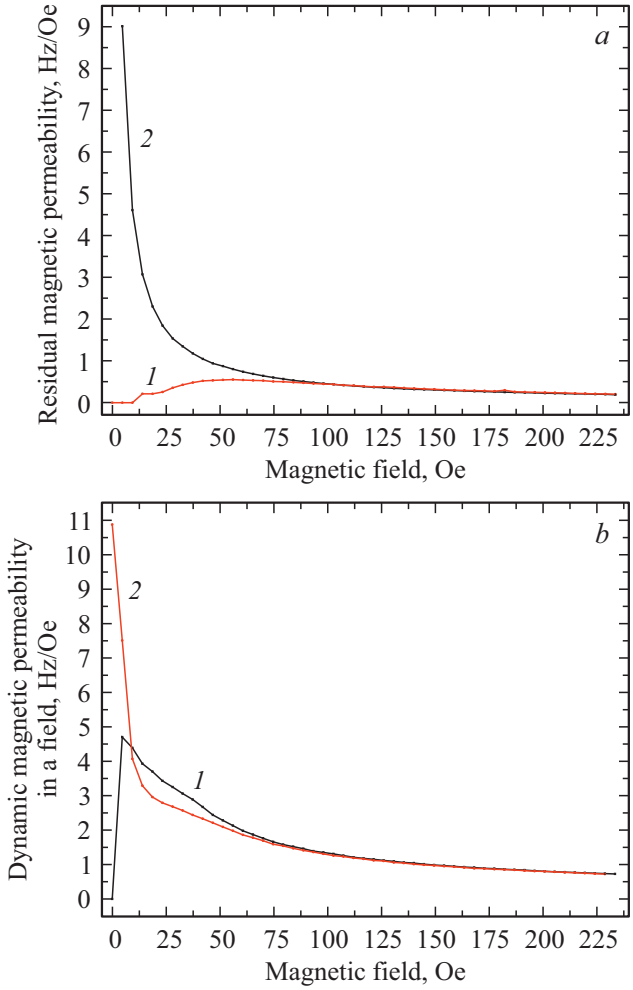

Figure 4. Field dependences of complex magnetic permeability of sample No. 1. (*a*) $\mu_{vtr}(H_0) = (B_{tr}/H_0)(H_0) \approx (\Delta f_{tr}/H_0)(H_0)$ with the external field switched off and only TMF being present in the sample; (*b*) $\mu_v(H_0) = (B/H_0)(H_0) \approx (\Delta f_u/H_0)(H_0)$ with the external magnetic field switched on. Curves *1* and *2* correspond to the increasing field and the decaying field, respectively. Temperature $T = 77.4$ K.

curves *1* in Fig. 4 through their maxima is governed by two conflicting processes. As the field increases in the region of weak fields, TMF first increases in superconducting loops, and then intertwine loop currents become suppressed by intertwine junction antivortices (ITJAVs) produced by Abrikosov vortices and ITJVs trapped at twins [19]. As a result, the curve goes through its maximum at field $H_{ic1} \approx 100$ Oe. Figures 1 and 2 illustrate well the linear sections of diamagnetic screening up to H_{ij}. When the field decreases, curves *2* in Fig. 4 in the region of weak fields demonstrate rapid linear growth induced by the diamagnetic screening of the external magnetic field from groups of superconducting loops. In the increasing field, curve *1* in Fig. 4, *a* also demonstrates linear growth up to $H_0 \approx 12.5$ Oe induced by the diamagnetic screening of the external magnetic field by macroscopic currents flowing

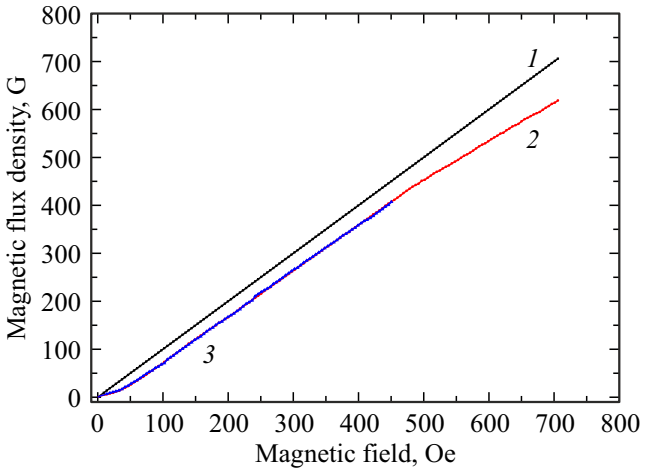

Figure 5. Typical field dependences of the magnetic flux density at the center on the surface of sample No. 1 measured with the HS: dependence $B_1(H_0)$ for the ZFC mode when the sample lacks a vortex lattice frozen in advance (curve *2*), dependence $B_2(H_0)$ for the ZFCMFA mode when the sample has a vortex lattice frozen in advance (curve *1*), and dependence $B_0(H_0)$ (curve *3*). The complete $B_{tr}(H_0)$ dependence is shown in the inset. The temperature is 77.4 K.

along the outside perimeter of the sample. The curve then goes through a sharp maximum due to the suppression of intertwine loop currents by ITJAVs and the emergence of an oppositely directed magnetic flux in the sample.

Figure 5 presents the typical field dependences of the magnetic flux density at the center on the surface of sample No. 1 measured with the HS: dependence $B_1(H_0)$ for the ZFC mode when the sample lacks a vortex lattice frozen in advance (curve *2*), dependence $B_2(H_0)$ for the ZFCMFA mode when the sample has a vortex lattice frozen in advance (curve *1*), and dependence $B_0(H_0)$ (curve *3*).

Figure 6 shows the typical field dependences of the local dynamic complex magnetic permeability of sample No. 1 measured with the HS. Dependence $\mu_v(H_0) = (B/H_0)(H_0)$ based on the data from Fig. 5 (curve *1* — ZFC mode, curve *2* — ZFCMFA mode) is presented in Fig. 6, *a*; dependence $\mu_{vtr}(H_0) = (B_{tr}/H_0)(H_0)$ based on the data from Fig. 5, *a* (curve *2* — ZFC mode, curve *1* — ZFCMFA mode) is plotted in Fig. 6, *b*; and dependence $\mu_v(H_0) = (B/H_0)(H_0)$ based on the data from Fig. 5, *a* (curve *1* — ZFC mode, curve *2* — ZFCMFA mode) is shown in Fig. 6, *c*. The fact that the superconducting glass state emerges in the sample is evidenced already at the level of interacting superconducting loops by the curves in Figs. 5 and 6, which go through the minimum in the region of weak fields when fluxes trapped in strong smaller-sized loops gradually suppress (as the field increases) currents of weak links of larger weak loops and flip the TMF direction in them. The averaged fields measured with the HS become alternating in sign as a result. Since TMF is measured after the removal of the external field, demagnetization fields induced by Meissner currents of twins, which interact with eddy currents of the vortex lattice frozen in advance in the sample and in its twins,

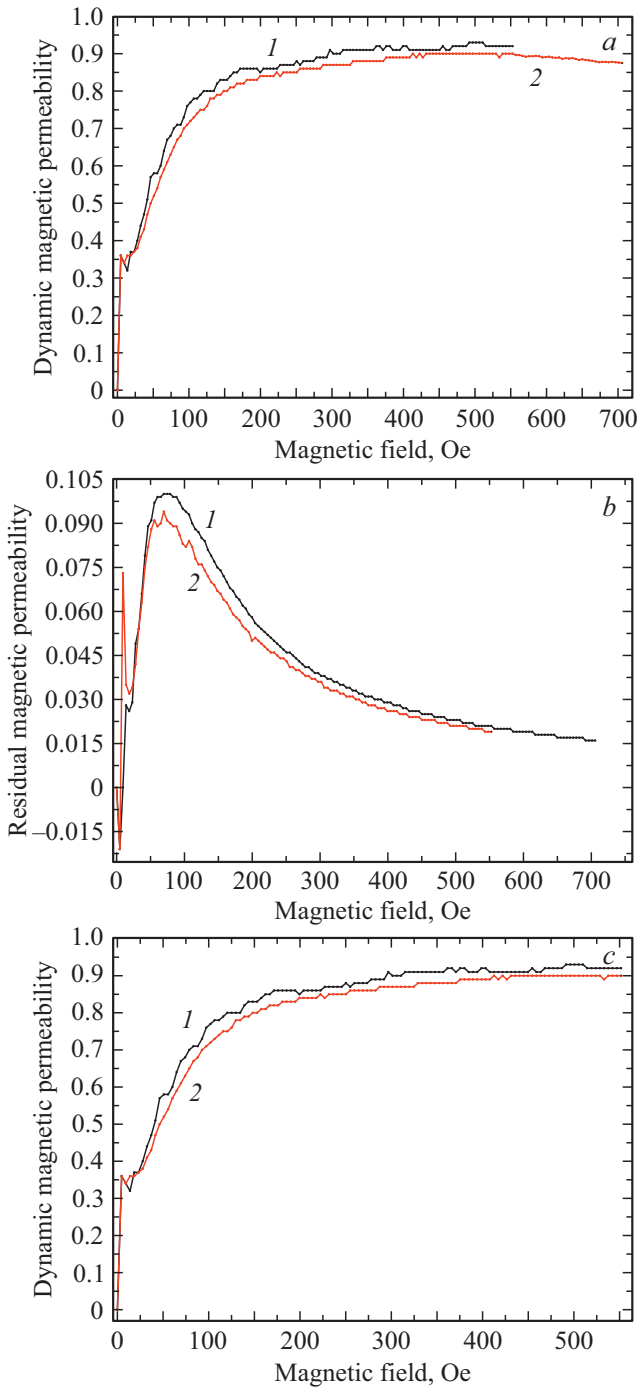

Figure 6. Typical field dependences of the magnetic permeability of sample No. 1 measured with the HS. (*a*) Dependence $\mu_v(H_0) = (B/H_0)(H_0)$ plotted based on the data from Fig. 5 (curve *1* — ZFC mode, curve *2* — ZFCMFA mode); (*b*) dependence $\mu_{vtr}(H_0) = (B_{tr}/H_0)(H_0)$ plotted based on the data from Fig. 5 (curve *2* — ZFC mode, curve *1* — ZFCMFA mode); (*c*) dependence $\mu_v(H_0) = (B/H_0)(H_0)$ plotted based on the data from Fig. 5, *a* (curve *1* — ZFC mode, curve *2* — ZFCMFA mode). Temperature $T = 77.4$ K.

remain in the end. A change in the Meissner phase–TB proportion leads both to the enhancement of the critical parameters of twins and to a more uniform distribution of strong local fields of similar magnitude between twins. Therefore, the sample decomposes into progressively finer twins (sub- and nanocrystallites) as the field increases, and these twins define the period of a more and more uniformly arranged vortex lattice [11,17–19]. Thus, the enhancement of short-range ordering induces a stepwise quantum phase transition from the vortex glass state to the Bragg glass state. The process of decomposition of the sample into progressively finer twins in the increasing external field allows one to determine the minimum TB distribution period and the minimum size of the unit cell of Bragg glass. In contrast to the artificial pinning center landscape [43,44], the gradual switching of TMF at natural periodically arranged pinning centers (TBs) in the present study allowed us to demonstrate the following:

(1) As the sample decomposes into twins in the increasing field, the TB distribution period decreases (quasi-periodically arranged pinning centers), and a landscape of pinning centers contracting in period with growing levels of local surface energies for entry of the next batch of vortices into the sample is produced.

(2) When the fields decreases, the pinning center landscape extends like a „sponge“, increasing the TB distribution period. Owing to the quantization of magnetic flux and the commensurability of the vortex lattice period and the quasi-periodic superstructure of weak links, the sample decomposition and the penetration of vortices are self-consistent. The discovered transformations in the vortex system are associated exactly with the manifestation of the glass-like nature of the crystallographic HTSC microstructure. As was demonstrated in [11,17–19], twins and TBs are also seen clearly in epitaxial films if a magnetic field is applied to them (another fine illustration of this is provided by Fig. 1). At the same time, if we take into account the results for bulk samples presented above, the following may be surmised. The undetectability of TBs in a film by common methods is attributable to the fact that small TBs are masked by extended dislocations, interdomain extended Josephson junctions, and other planar defects [24,25]. The magnetic field and TMF suppress intertwine weak Josephson links, and the demagnetization fields of twins close via TBs around twins, forming oppositely directed dipoles and thus producing the needed contrast for TB detection in a film [11,17–19]. The increase in magnitude of the field results only in shortening of longer weak links (TBs) and transformation of spatial scales of Josephson vortices. As Josephson vortices become smaller, they start being sensitive to neighboring short TBs and small-scale structural nonuniformities of the sample.

That said, it should also be noted that long second-generation YBCO HTSC tapes [45] carry current in the region of strong external transverse magnetic fields and intrinsic fields of currents flowing through the tape (inducing strong external and internal demagnetization fields due to the high demagnetization factor of the film). Although this current is smaller in amplitude than the critical currents of epitaxial films on smaller substrates, it is still sufficient for the use of such tapes in high-current superconductivity. This raises a number of questions regarding the common nature of twins and TBs in different types of YBCO HTSC having various designs and fabricated using different techniques. In our view, the nature of relatively high critical currents carried by these tapes in strong intrinsic and external magnetic fields is as follows.

(1) Owing to the high n value of a second-generation YBCO HTSC tape, the film in a magnetic field perpendicular to its surface decomposes into progressively finer sub- and nanocrystallites. As a result, the degree of suppression of intertwine critical currents J_c by external and internal demagnetization fields of twins, which were induced in the film by the external transverse field and the intrinsic field of the current flowing through it, decreases. Thus, the enhancement of suppression of J_c by the increasing external magnetic field and the field of current flowing through the tape is compensated by the weakening influence of internal demagnetization fields of twins (due to the reduction of n of twins) on J_c. The enhancement of critical parameters and short-range ordering in the glass-like crystalline structure of the tape film also contributes to a high J_c value [11,17–19]. The formation of a network of flow channels containing small-angle boundaries in the film is another factor contributing to a high J_c [45].

(2) As was demonstrated in [19], rigidly fixed ITJVs and ITJAVs, which differ in shape from Abrikosov vortices and may vary in size (become smaller as the field increases), form at TB intersection points. In addition, the positions of Abrikosov and Josephson vortices in the space between ITJVs and ITJAVs are also fixed rigidly. This leads to a considerable suppression of heating of intertwine weak contacts in the process of motion of nonmobile ITJVs, ITJAVs, and Abrikosov and Josephson vortices. Therefore, the influence of thermal effects due to the thermally activated flux creep on J_c decreases.

(3) Since the major issues pointed out in paragraphs (1) and (2) are minimized, the remaining insignificant processes affecting J_c are shunted by an interlayer and a metal substrate of second-generation superconducting tapes.

(4) As was demonstrated in [2–5] and above, single-crystalline grains of polycrystalline YBCO HTSC and single-crystalline YBCO HTSC contain a great number of TBs. Therefore, although they may be assumed to be single-crystalline as a first approximation, it is actually not true. According to known facts and the obtained data presented above (see Section 2.1.1), the critical currents of YBCO samples at $T = 77.4\,\mathrm{K}$ in the terrestrial field are $\approx 5.7 \cdot 10^3\,\mathrm{A/cm^2}$ (quasi-single-crystalline samples); $\approx 6 \cdot 10^5\,\mathrm{A/cm^2}$ (monodomains); $\approx 5 \cdot 10^6\,\mathrm{A/cm^2}$ (epitaxial films), $\approx 2.2 \cdot 10^6\,\mathrm{A/cm^2}$ (four-layer YBCO — interlayer — YBCO second-generation HTSC tapes with a thickness of $1\,\mu\mathrm{m}$ [46]). These currents are much lower than depairing current $J_c^{GL}(77.4) \approx 1.91 \cdot 10^7\,\mathrm{A/cm^2}$ in the terrestrial field.

In addition, as was demonstrated in [11,17,18], the value of J_c changes in an increasing field from $\approx 5.7 \cdot 10^3$ A/cm^2 for the sample to $\approx 8.2 \cdot 10^7$ A/cm^2 for sub- and nanocrystallites ≈ 81 nm in size in field $H_c \approx 2.82 \cdot 10^3$ Oe. It can be seen that the currents for sub- and nanocrystallites in field $H_c \approx 2.82 \cdot 10^3$ Oe are more than two orders of magnitude higher than the critical current of a monodomain measured using the four-probe method in the terrestrial field and are higher than J_c^{GL}. These data suggest that although the critical currents of weak links increase as twins become smaller in size, they still decompose into smaller twins. The similarity of results corresponding to samples with different microstructures, morphologies, geometric sizes, shapes, and fabrication techniques also indicates that they feature a universal mechanism of flux entry (exit), distribution, and trapping. Therefore, the presence of both weak links and twinning is likely to be a fundamental property of YBCO HTSC.

4. Conclusion

Thus, integral and local measurements of the dynamic complex magnetic permeability of bulk and film YBCO HTSC samples clearly indicated that they may undergo stepwise decomposition into groups of twins with close n, inducing stepwise penetration of the magnetic flux into the sample. It was verified that the stepwise decomposition of the sample into twins and the stepwise flux penetration are of a bulk nature in both film and bulk samples. Therefore, although penetration depth 2λ in films is close in magnitude to the film thickness, quantum size effects related to the film thickness are excluded. The obtained results suggest that the lattice symmetry competition in transition from the tetragonal phase to the orthorhombic one results in the formation of a group of twins with quantized spatial scales in the sample. The steps in field dependences $B_{tr}(H_0)$, $B(H_0)$, $(\Delta f_{tr})(H_0)$, $(\Delta f_u)(H_0)$, $\mu_{vtr}(H_0)$, and $\mu_v(H_0)$ are manifested vividly in formation of the vortex lattice due also to the quantization of magnetic flux and the quantized period change of the vortex lattice of TBs pinned quasi-periodically in the sample. As the field increases (decreases), a discretely contracting (extending) quasi-periodic landscape of pinning centers with higher (lower) local edge barriers for entry (exit) of the next batch of vortices forms. This leads to a more and more ordered arrangement of small TBs and enhances short-range ordering in the vortex lattice, thus providing for a stepwise quantum phase transition from the state of a vortex glass to the state of a Bragg glass. It is of fundamental importance to determine the ratio of unit cells of the crystalline HTSC structure and the vortex Bragg glass formed in it.

Funding

This study was financed from the budget under the state assignment, project No. 0030-2019-0014.

Conflict of interest

The author declares that he has no conflict of interest.

References

[1] J.G. Bednorz, K.A. Muller. Z. Phys. B **64**, 189 (1986).
[2] Y. Syono, M. Kikuchi, K. Oh-ishi, K. Hiraga, H. Arai, Y. Matsui, N. Kobayashi, T. Sasaoka, Y. Muto. Japn. J. Appl. Phys. **26**, L498 (1987).
[3] G. Roth, D. Ewert, G. Heger, M. Hervieu, C. Michel, B. Raveau, F. D'Yvoire, A. Revcolevschi. Z. Phys. B **69**, 21 (1987).
[4] S. Nakahara, T. Boone, M.F. Yan, G.J. Fisanick, D.W. Johnson. J. Appl. Phys. **63**, 451 (1988).
[5] A.A. Abrikosov, A.I. Buzdin, M.L. Kulic, D.A. Kuptsov. J. Exp. Theor. Phys. **68**, 210 (1989).
[6] I.N. Khlyustikov, A.I. Buzdin. Sov. Phys. Usp. **31**, 409 (1988).
[7] V.V. Shmidt. Vvedenie v fiziku sverkhprovodnikov. Mosk. Tsentr Nepreryvnogo Mat. Obraz., M. (2000) (in Russian).
[8] Yu.M. Tsipenyuk. Fizicheskie osnovy sverkhprovodimosti. Fizmatkniga, M. (2003) (in Russian).
[9] M. Eisterer. Phys. Rev. B **99**, 094501 (2019).
[10] Y.-H. Zhou, C. Wang, C. Liu, H. Yong, X. Zhang. Phys. Rev. Appl. **13**, 024036 (2020).
[11] Kh.R. Rostami. Low Temp. Phys. **177**, 99 (2014).
[12] Kh.R. Rostami, I.P. Nikitin. **153**, 107423 (2020).
[13] B. Kalisky, J.R. Kirtley, J.G. Analytis, Jiun-Haw Chu, A. Vailionis, I.R. Fisher, K.A. Moler. Phys. Rev. B **81**, 184513 (2010).
[14] J.R. Kirtley, B. Kalisky, L. Luan, K.A. Moler. Phys. Rev. B **81**, 184514 (2010).
[15] B. Kalisky, JR Kirtley, JG Analytis, Jiun-Haw Chu, I.R. Fisher, Kathryn A. Moler. Phys. Rev. B **83**, 064511 (2011).
[16] John M. Tranquada. Physics **3**, 41 (2010).
[17] Kh.R. Rostami. JETP Lett. **105**, *12*, 792 (2017).
[18] Kh.R. Rostami. Int. J. Mod. Phys. B **32**, *31*, 1850346 (2018).
[19] Kh.R. Rostami. JETP Lett. **108**, 734 (2018).
[20] A.S. Mel'nikov, Yu.N. Nozdrin, I.D. Tokman. Phys. Rev. B **58**, 11672 (1998).
[21] A.Yu. Aladyshkin, A.K. Vorob'ev, P.P. Vysheslavtsev, E.B. Klyuenkov, A.S. Mel'nikov, Yu.N. Nozdrin, I.D. Tokman. J. Exp. Theor. Phys. **89**, *5*, 940 (1999).
[22] M.S. Afanas'ev, A.N. Bazlov, V.N. Gubankov, I.M. Kotelyanskii, V.A. Shakhunov. Radiotekhnika *10*, 88 (2005) (in Russian).
[23] A. Kuhle, J.L. Skov, S. Hjorth, I. Rasmussen, J. Bindslev. Hansen. Appl. Phys. Lett. **64**, *23*, 3178 (1994).
[24] Kh.R. Rostami. Am. J. Mod. Phys. **2**, *1*, 21 (2013).
[25] Kh.R. Rostami. Phys. Solid State **55**, *9*, 1786 (2013).
[26] A.M. Campbell, J.E. Evetts. Critical Currents in Superconductors. Monographs on Physics. Taylor and Francis Ltd, London (1972). 243 p.
[27] Kh.R. Rostami. Instrum. Exp. Tech. **59**, *2*, 273 (2016).
[28] Kh.R. Rostami. Tech. Phys. **65**, *12*, 1975 (2020).
[29] G. Deutsher. Physica C **153**–**155**, 15 (1988).
[30] H. Dersch, G. Blatter. Phys. Rev. B **38**, 11391 (1988).
[31] C. Ebner, D. Stroud. Phys. Rev. B **31**, 165 (1985).
[32] G. Deutcher, K.A. Muller. Phys. Rev. Lett. **59**, 1745 (1987).
[33] Ankit Kumar, Sayantan Ghosh, Tsuyoshi Tamegai, S.S. Banerjee. Phys. Rev. B **101**, 014502 (2020).

[34] D. Bazeia, M.A. Liao, M.A. Marques, R. Menezes. Phys. Rev. Res. **1**, 033053 (2019).
[35] D.K. Nelson. Phys. Rev. Lett. **60**, 1973 (1988).
[36] M.P.A. Fisher. Phys. Rev. Lett. **62**, 1415 (1989).
[37] A. Zippeliuse, B.I. Halperin, D.R. Nelson. Phys. Rev. B **22**, 2514 (1980).
[38] S. Scheide, V.M. Vinokur. Phys. Rev. B **56**, 8522 (1997).
[39] V.M. Geshkenbein, L.B. Ioffe, A.I. Larkin. Phys. Rev. B **48**, 9917 (1993).
[40] T. Giamarchi, P. Doussa. Phys. Rev. Lett. **72**, 1530 (1994).
[41] T. Giamarchi, P. Doussal. Phys. Rev. B **52**, 1242 (1995).
[42] E.B. Sonin. JETP Lett. **47**, 496 (1988).
[43] Y. Schlussel, T. Lenz, D. Rohner, Y. Bar-Haim, L. Bougas, D. Groswasser, M. Kieschnick, E. Rosenberg, L. Thiel, A. Waxman. Phys. Rev. Appl. **10**, 034032 (2018).
[44] G. Zechner, W. Lang, M. Dosmailov, M.A. Bodea, J.D. Pedarnig. Phys. Rev. B98, 104508 (2018).
[45] Second-Generation HTS Conductors / Ed. A. Goyal. Kluwer Academic. (2005). 347 pp.
[46] M.Ya. Garaeva, I.A. Chernykh, T.S. Krylova, R.I. Shainurov, E.P. Krasnoperov, M.L. Zanaveskin. Tech. Phys. Lett. **40**, *10*, 905 (2014).